In situ observation of microscopic damage and crack initiation mechanisms in a filled EPDM

Jesbeer Kallungal, Laurent Chazeau, J.-M. Chenal, Jérôme Adrien, E Maire, Claire Barrès, Bernard Cantaloube, Patrick Heuillet, Fabien Wilde, Julian Moosmann, et al.

▶ To cite this version:

Jesbeer Kallungal, Laurent Chazeau, J.-M. Chenal, Jérôme Adrien, E Maire, et al.. In situ observation of microscopic damage and crack initiation mechanisms in a filled EPDM. Engineering Fracture Mechanics, 2023, 277, pp.109007. 10.1016/j.engfracmech.2022.109007 . hal-03912973

HAL Id: hal-03912973
https://hal.science/hal-03912973v1

Submitted on 26 Dec 2022

In situ observation of microscopic damage and crack initiation mechanisms in a filled EPDM

Jesbeer Kallungal[1,2,3,]*, Laurent Chazeau[1,]*, Jean-Marc Chenal[1], Jérôme Adrien[1], Eric Maire[1], Claire Barrès[2], Bernard Cantaloube[3], Patrick Heuillet[3], Fabien Wilde[4], Julian Moosmann[4], Timm Weitkamp[5]

[1]*Univ Lyon, INSA Lyon, CNRS, MATEIS UMR5510, F-69621, Lyon, France*

[2]*Univ Lyon, INSA Lyon, CNRS, IMP UMR5223, F-69621, Lyon, France*

[3]*LRCCP, F-94408, Vitry-sur-Seine, France*

[4]*Helmholtz-Zentrum Hereon, Max Planck Strasse, 21502 Geesthacht, Germany, Germany*

[5]*Synchrotron SOLEIL, F-91190 Saint-Aubin, France*

Corresponding authors: laurent.chazeau@insa-lyon.fr

ABSTRACT

The paper presents a precise 3D quantification of damage evolution and eventual crack initiation due to metallic oxide particles and filler agglomerates in a peroxide crosslinked filled EPDM during uniaxial solicitation, thanks to synchrotron radiation X-Ray Tomography. An in-situ tensile study using this technique reveals polymer debonding at the poles of all metallic oxide particles upon stretching. The cavities caused by this decohesion do not lead to crack initiation since they grow parallel to the applied stress direction. Conversely, crack always initiates from carbon black agglomerates (CB_{aggl}). The crack initiation mechanism is a three step process that begins with the nucleation of cavities *inside* the CB_{aggl} upon stretching. This is followed by the growth of these cavities which brings about the fracture of the agglomerates. Finally, this fracture can lead to the creation of a matrix crack at the origin of the material rupture. It is also confirmed that CB_{aggl} that initiate the critical crack in the material are the biggest sized CB_{aggl} and are located close to the edges of the sample.

1. INTRODUCTION

In various applications, elastomers are required to withstand high strain deformation during different types of solicitations. Incorporation of reinforcing fillers is an efficient way to improve their rupture and fatigue properties during such solicitations[1–3]. If the fillers disperse improperly, they will remain as filler agglomerates. The existence of these agglomerates is inevitable in industrially produced materials[4,5]. They are known to be crack precursors and are considered as defects in elastomer materials. Apart from these, there are other defects like metallic oxides particles, micro-bubbles and voids of different shapes [3,6–9]. The latter appear in the matrix, mostly at the poles of the defects. There is a competition between cavitation mechanism and decohesion mechanism (void formation originating from the debonding between the polymer and the rigid inclusions), depending on the adhesion strength between the matrix and the inclusion [8,10–12]. These damage mechanisms, for instance decohesion at the poles of ZnO metallic particles and cavitation in the polymer between filler agglomerates, have been observed in industrial rubber compounds, [8,9]. Post mortem analysis using electron microscopy reveals agglomerates at the crack initiation sites in a ruptured material [6,8]. Huneau *et al.*[8] have suggested that crack initiation from a filler agglomerate is due to cavity growth from its pole. However, this is contrary to the observations made by Gent *et al.*[10] and Lefèvre *et al.*[13], who studied material rupture in the presence of more than one rigid inclusion. They noticed that cavity growth at the midpoint distance between two inclusions leads to rupture rather than decohesion at their poles. Thus, there is no agreement in the literature on the mechanisms which allow the transition from local damage (cavitation or decohesion) associated to a defect, to a crack leading to the material ruptures , especially for carbon black agglomerates (CB_{aggl}) in an industrial rubber compound. Such study requires a precise 3D quantification and visualization of the damage initiation, its evolution and the eventual crack initiation resulting from this damage.

To do so, we studied the rupture properties of 3 model materials with same rubber formulation containing a fixed low concentration of metallic particles (detected by tomography) and varying volume fraction of CB_{aggl}. We performed an in-situ tensile study on these materials using Synchrotron Radiation Computed Tomography (SRCT). SRCT has been chosen compared to lab X-ray tomography as it enables better phase contrast, spatial and time resolution[14,15]. When performed concomitantly with mechanical testing, tomography enables a direct observation of damage mechanisms associated to defects like metallic oxide particles and CB_{aggl}, the damage evolution and crack formation inside the material. This analysis enables to extract various features controlling crack initiation mechanism such as the morphology and the location of the critical defects at the origin of the material rupture.

2. MATERIALS AND TESTING

2.1 Composition and materials processing

Model materials used for the current study are based on a non-crystallizing Ethylene Propylene Diene Monomer rubber (EPDM Keltan 4450) reinforced with high furnace carbon black (N326) and cross-linked using unsupported Bis (α,α-dimethylbenzyl) peroxide. The composition of the materials (Table 1) was kept constant whereas compounding process conditions were varied in order to generate more or less defects inside them. This specific composition enables the generation of CB_{aggl} defects. All the ingredients except the peroxide were mixed in a Haake Rheomix 600 OS mixer (chamber volume: $120 cm^3$) using Banbury rotors ($42\ cm^3$) at a certain rotor speed and mixing time (Table 1), and were then passed 10 times in a two-roll mill where the peroxide was added. The sequence of ingredients addition is detailed in Table 1. USD method refers to “upside down”, i.e., the elastomer was added after carbon black, TD method refers to “top down”, i.e., carbon black was introduced after the elastomer in the internal mixer. After processing the material in the internal mixer and the two-roll mill machine, the samples were molded as a 1 mm thick sheet at 170°C under 190 MPa for 12 min. Curing time (t98) was estimated from torque measurements performed using a Monsanto rheometer analyzer. The samples for mechanical tests were die cut from this sheet using pneumatic punching tool. Hereafter, the samples are named S_X with X corresponding to the volume fraction of CB_{aggl} with a volume larger than 125 μm^3. This minimum value is dictated by the tomography resolution and corresponds to the value under which the error on the evaluation of the agglomerates volume is too important.

Table 1: Composition of the Model Materials and processing conditions

Samples	S_11.5	S_9.0	S_4.3
Ingredients	(Phr)	(Phr)	(Phr)
EPDM Keltan 4450	100	100	100
Carbon Black	50	50	50
Peroxide	3.2	3.2	3.2
Rotor Speed (rpm)	30	30	60
Mixing Time (min)	2	2	4
Introduction Protocol	TD	USD	USD
Filler Volume fraction	19.3%	19.3%	19.3%

2.2 Scanning electron microscopy (SEM)

We characterized the rupture surface of the materials by SEM using Zeiss Supra SEM (Germany). The materials were not metallized to avoid any closing of the crack. Observation of non-metallized surfaces requires low acceleration voltage to avoid any accumulation of charges. Thus, the energy of the electron beam was kept at 1 kV. The detector used is secondary electron detector. The composition of defects was obtained using Energy Dispersive X-Ray (EDX) detector. EDX needs a higher acceleration voltage of 10 kV for a higher emission of characteristic X-ray from the material surface.

2.3 Synchrotron radiation computed tomography (SRCT)

SRCT experiments were performed at the PETRA III P05 beamline at DESY[16], Germany (operated by Helmholtz-Zentrum Hereon), and the Anatomix beamline at SOLEIL, France. We obtained information regarding the onset of damage and crack initiation mechanism using both beamlines. At P05 imaging beamline, the energy of the monochromatic X-rays was 15keV with a spatial resolution of 2.19µm. The sample was mounted in a tensile rig (see Figure 1a in reference[17]). Its specific geometry (Figure 1) was designed to create as high stress as possible in the region of interest (ROI). The sample was rotated over 360° by steps of 0.225°. Each projection step lasted 30ms resulting in a total time per scan of 50s. We reconstructed 3D images with and without phase contrast. Images without phase contrast were used for the detection of damage (CB_{aggl} fracture and cavities) in the materials during the test. Then the CB_{aggl} associated to damage were segmented from the images acquired with phase contrast. This contrast was obtained by applying a phase retrieval algorithm implemented by Moosmann et al. [18]. Experiments performed at Anatomix @SOLEIL[19,20] used a filtered white beam with a mean energy of 20keV and a spatial resolution of 1.3µm. We used a homemade tensile rig with 5kN load cell for the tensile tests (see Figure 1c in reference [21]) . The sample was rotated over 360° by steps of 0.18°. Each projection required 150 ms resulting in a total time per scan of 360s. At Anatomix, we improved the phase contrast of the image by applying Pagnanin filter before the 3D volume reconstruction[22].

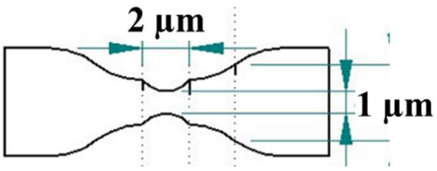

Figure 1: Sample geometry used for in-situ tensile test

After the reconstruction, we performed image analysis to optimize the contrast and to remove additional noise. The reference [23] reports the details of the protocol. Each agglomerate is labelled in the binary image after its segmentation from the matrix. Its geometric features such as Volume V, Equivalent Diameter Eq_{diam}, Length of major principle axis a, Length of minor principle axis b and Eccentricity E are extracted using the regionprops module[24] in Python. The volume V of a CB_{aggl} is proportional to the number of voxels it contains (1 voxel=10.50μm^3). The Equivalent diameter (Eq_{diam}) represents the diameter of a fictive inclusion having the same volume as the analyzed CB_{aggl}. Length of major (a) and minor principal axis (b) are those of an ellipsoid that has similar normalized 2nd central moment as the CB_{aggl}. Eccentricity (E) of an ellipse is the ratio between the distance of its two foci and the major principal axis length. Here, E is the eccentricity of the centered elliptic section of the ellipsoid, perpendicular to the c axis (with a > c > b): $= \sqrt{1 - b^2/a^2}$. The bulk factor (B) of an agglomerate corresponds to the ratio of the free space (volume in this case, ΔV) between the agglomerate and the convex hull constructed around it to the total volume of the convex hull (V_{ch}), i.e. $B(\Delta V) = 1 - V/V_{ch}$.

2.4 Tensile testing

Tensile tests were conducted on an MTS 1/ME machine equipped with a 100N load cell. The nominal stress is defined as $\sigma_n = F/S_0$, where F is the force and S_0 is the initial section of the sample. In most cases, true stress is used, which is defined as $\sigma(t) = F(t)/S(t)$ where S(t) is the current section area of the sample. In elastomeric materials whose deformation is isochoric, the true stress can be defined as $\sigma_n(1 + \epsilon_n)$, where σ_n is the nominal stress and ϵ_n is the nominal strain defined as $\epsilon_n = \frac{\Delta L}{L_0}$ (L_0 is the nominal length and ΔL is the displacement). The nominal strain is obtained using digital image correlation. The strain rate was around 0.005 s^{-1}. The geometry of the sample used for tensile tests is presented in Figure 1. All the experiments were conducted at room temperature (25°C+/- 2°).

2.5 Digital volume correlation

Digital Volume Correlation (DVC) is a correlation methodology to measure the 3-dimensional displacement and strain field inside a material volume during a solicitation (e.g. compression, tension etc.) The principle used in DVC is derived from DIC, where the displacement vector of each voxel in the volume subset is obtained and is used to calculate the strain field. The analysis was performed using a routine developed by Joel Lachambre in his Ph-D thesis [25]. A ROI of 400*300*200 voxels has been defined within a sample volume of 850*1000*500 voxels. In order to have a good correlation, the step displacement during tensile test is limited to 40 µm The chosen size of the mesh is 16 voxels. The resolution of the voxel is 2.19µm^3. During the analysis, a continuous displacement field is measured when discretized over a finite element mesh made of 8-noded (C8) cubes[26]. The mean green Lagrange strains are computed over each element associated with the C8 discretization. ϵ_{yy} is the strain along the tensile direction.

3. RESULTS

3.1 Microstructural characterization of different defects

Filled EPDM contains mainly 2 kinds of defects, pre-existing metallic particles in the polymer and non-dispersed CB_{aggl}. As illustrated in Figure 2, the metallic particles have high greyscale values, which indicates that they are made of elements with higher atomic number than carbon. EDX analysis confirms that they are metallic oxides (Na_2O or K_2O). ~~(SI 7.2).~~ Their volume fraction is around 0.03-0.05% in the 3 model materials. Their average and largest Eq_{diam} are 7.5µm and 32µm, respectively.

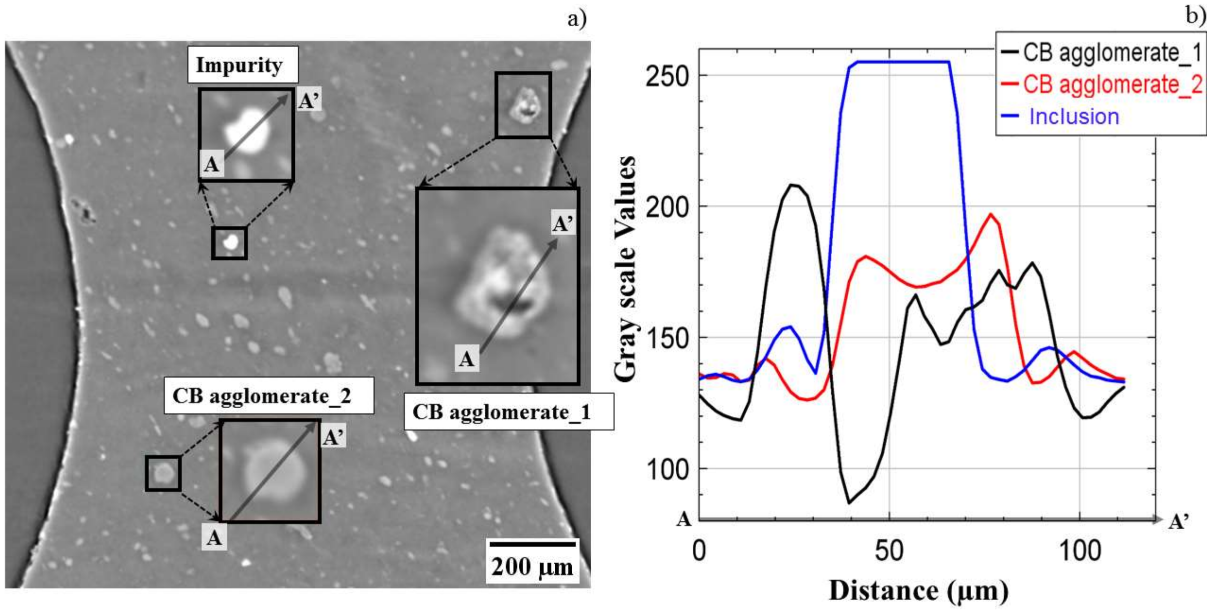

Figure 2: a) slice view of ROI of an S_9.0 test sample. Zoomed areas correspond to a metallic particle and two CB_{aggl}. The grey scale intensity values across the lines drawn through these defects are plotted in b).

CB_{aggl} can be clearly distinguished from the matrix owing to the phase contrast imaging techniques implemented at P05 beamline. The two agglomerates presented in Figure 2 have different densities. CB_{aggl_1} has a lower density at the center than CB_{aggl_2} since there is a drop in greyscale values in its center. CB_{aggl_2} is the most frequently observed type of agglomerate in the material. In our previous article[17], we have shown that these agglomerates are made of local over concentration of aggregates inter penetrated by elastomer through TEM analysis. The smaller electronic density of CB_{aggl_1} can be due to a lower concentration of aggregates and the possible presence of voids. In any case, all the detected agglomerates are deformable clusters in which concentration of aggregates varies locally. The volume fractions of CB_{aggl} with a volume above 125µm^3 are 11.5%, 9% and 4.3% , in S_11.5, S_9.0 and S_4.3 respectively. The corresponding mean Eq_{diam} of these CB_{aggl} populations are 10.8µm, 11.0µm and 11.1µm respectively. The distribution of their structure factor shows that CB_{aggl} in S_11.5 are the most structured and those is S_9.0 are the least structured (see reference [23] for the protocol analysis of similar sample prepared with the same process).

3.2 Tensile properties

Figure 3 shows the stress-strain curve obtained for the 3 model materials using the sample geometry in Figure 1. The mechanical properties are not affected by the concentration of CB_{aggl}, like already observed for planar geometry (PS) geometry specimens[17]. All the materials have similar strain and stress at break (Figure 4).

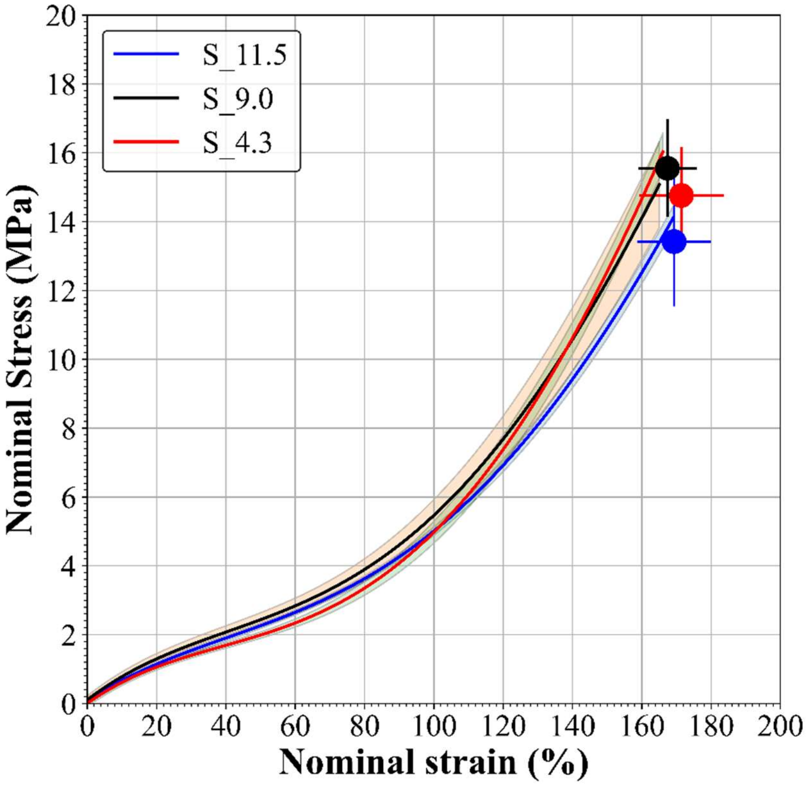

Figure 3: a) nominal stress vs nominal strain for the 3 materials with different concentrations of CB_{aggl}. Filled circles (blue: S_11.5, black: S_9.0, red: S_4.3) in the graph denotes the nominal stress and nominal strain at break for the 3 materials.

3.3 Damage mechanisms associated to the different types of defects

3.3.1 Visualization of damage mechanism

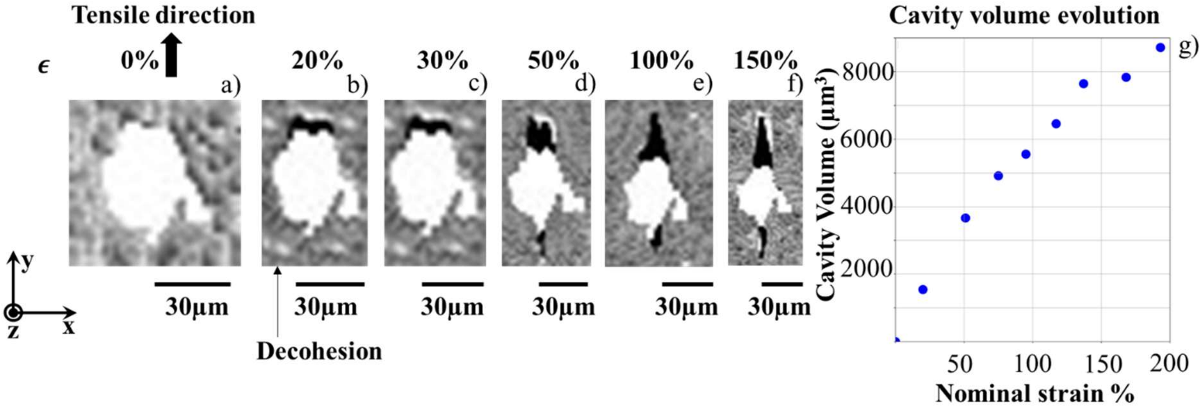

Figure 4: a)-f): damage evolution around a metallic particle with V= 18000µm^3 (Eq_{diam} = 32µm) as a function of deformation: b) decohesion, e) and f) cavity growth in the direction of the applied stress, g) cavity volume around this particle, as a function of nominal strain.

Figure 4 shows the slice view of a metallic particle with V= 18000µm^3 (Eq_{diam} = 32µm) inside the material during its tensile testing. These particles are rigid, they do not deform during the experiment and do not fracture like observed in other studies with ZnO particles (see [27], and the SI in section 7.1 which shows ZnO fracture in a material in which 3% ZnO was incorporated). As the material deforms, decohesion occurs at the poles of the particles since they have a weak adhesion with the matrix. The evolution of the interface is observed at every 1% strain, using X-ray tomography scan to determine the onset of decohesion at the poles of the particle. This decohesion appears as black pixels at the interface. Note that one may think from figure 4 that the particle surrounding has already a lower density, even without applied deformation. However, this is an artifact related to the strong phase contrast between the polymer and the particle. This artifact can be distinguished from void when comparing the evolution of the images with strain (said differently, this apparent lower density does not look like void). To avoid any misinterpretation, it requires a careful examination of the images, which is therefore very time consuming.

Decohesion can occur at the early stages of deformation, depending on the size of the particle. Moreover, in the case of figure 4, the cavity volume increases with the strain up to around 135%, then slows down. We have found that the smaller the particle, the sooner the cavity volume stabilizes: as an example, as shown in SI section 7.2, it does at 90% nominal strain for a V=6700µm^3 (Eq_{diam} of 23µm).

The damage in CB_{aggl} was already described in a previous article[17]: cracks and voids appear *inside* the agglomerates at a certain applied strain. Upon further stretching, more cracks appear within the agglomerates. Most of the CB_{aggl} undergo this damage sooner or later. Similar damage evolution was also observed in S_9.0 material (see SI section 7.3).

3.3.2 Decohesion onset

Besides the strain at which decohesion between metallic oxide particle and polymer occurs, the corresponding stress can also be analyzed (Figure 5). The comparisons are made with Eq_{diam} instead of V for an easy understanding.

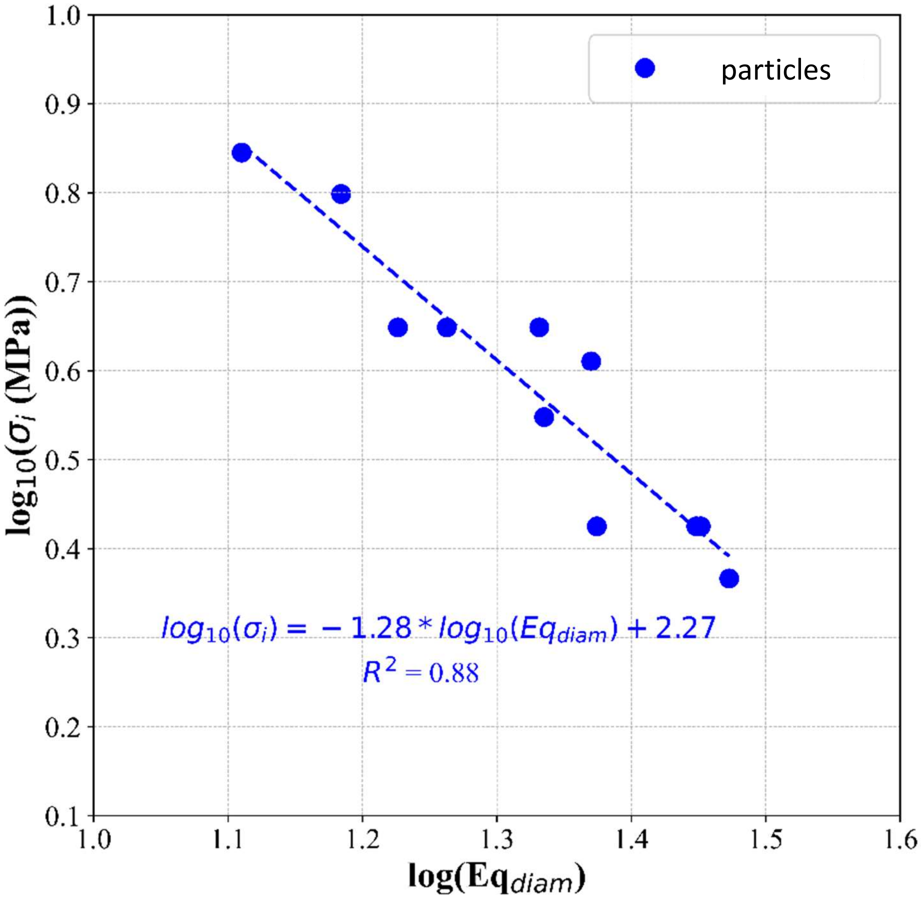

Figure 5: log plot of evolution of true stress at the decohesion onset (σ_i) with the Eq_{diam} of the metallic particle (S_4.3 material). Dotted line for the linear curve fitting.

The plot of macroscopically applied true stress σ_i at the onset of decohesion for metallic particles of different Eq_{diam} (Figure 5) clearly shows that smaller particles require higher macroscopic stress for decohesion, as often reported in literature[11,12,28–30]. The stress at the decohesion onset depends on the size of the debonded zone. If one assumes that the stress depends only on the square root of the diameter of the inclusion and that the bond fracture surface area is independent of the particle size – like Gent *et al.*[12] did for the decohesion from spherical inclusion- then one should find a linear dependence of σ_i with $Eq_{diam}{}^{-0.5}$. As shown in Figure 5, the curve fitting rather indicates a dependence with $Eq_{diam}{}^{-1.28}$. This discrepancy is not so surprising since the model relies on strong assumptions (spherical inclusions) whereas the metallic particles observed here are very irregular. Actually, the good quality of the fit is more surprising.

Similarly, the onset of cavitation (i.e. crack and void growth) inside the agglomerates is correlated to the true macroscopic stress, as shown on Figure 6.

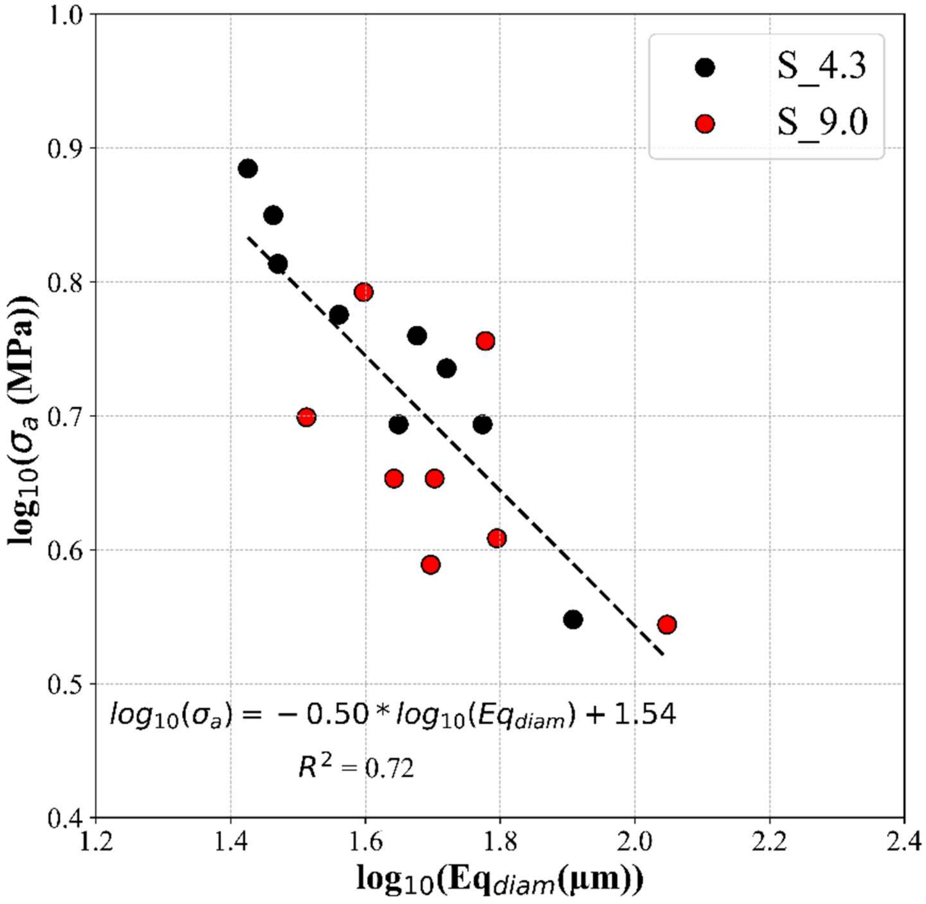

Figure 6: applied true stress at the cavitation onset (σ_a) as a function of the Eq_{diam} of the agglomerate in which it occurs (results from S_4.3 and S_9.0 materials). Dotted line for the linear curve fitting. Each point in the figure represents an agglomerate either from the material S_4.3 or S_9.0 (Note that this already represents a huge amount of work as it requires a careful examination of many images, to avoid any misinterpretation of artifacts).

As shown in Figure 6, the linear curve fitting is satisfactory and suggests a dependence of σ_a on $Eq_{diam}^{-0.5}$. Moreover in this figure, one can see that the linear dependence of log(onset stress) with the log(Eqdiam) is more convincing for the data taken from the S_4.3 material than for the S_9.0 material. This is not surprising as the larger quantity of agglomerates in the latter increases the probability for the agglomerates to be close to each other and therefore the probability for their stress/strain fields to be perturbed by their neighbors. Thus, this make less relevant the description of each agglomerate as an isolated one in an infinite medium submitted to a macroscopic tensile stress. In other word, this may explain the scattering of the data. The cavity being created *inside* the agglomerates, the Gent model previously cited seems irrelevant to explain these results. One may rather use the Mossakovskii and Rybka description (which is actually not so far from the Gent description), which derives the stress for the detachment of an elastic half space from a rigid plate when a circular debond of radius *a* occurs at the interface. It predicts a dependence with $a^{-0.5}$. We have indeed observed that the structure of agglomerates is very heterogeneous and may be described like an assembly of strong aggregate layers separated by soft polymer layers. In this description, the largest layers, close to the equator of the agglomerate (the poles indicating the tensile stress direction), are the ones where the void formation (originating here from decohesion) is the easiest[31] and have indeed a circular surface with a radius close/proportional to the radius of the agglomerate. Some similarities can also be found with the mechanisms of voids nucleation and growth observed in a semi crystalline polyamide 6 specimen undergoing tensile deformation[32].

3.4 Visualization of crack initiation

The transition from a fracture within a CB_{aggl} towards a crack inside the matrix has been visualized by tomography. This is illustrated on Figure 7 with the S_9.0 material. Note that the agglomerate shown in Figure 7a is of the same type as CB_{aggl_1} in Figure 2 i.e. it has a lower density compared to most of the observed agglomerates. The greyscale values show that its core is less dense. Nevertheless the observations on this agglomerate are very similar to those performed on other samples, and have been preferred for the quality of the images (see another example in SI section 7.4). The crack initiation in the agglomerate occurs at around 75%

nominal strain for this CB_{aggl} whose Eq_{diam} is 40µm. This crack inside the agglomerate transforms to a crack in the matrix at around 130% nominal strain. Such crack can then propagate through the material. Figure 7d shows the state of the crack inside the matrix just before material rupture. The evolution of nominal strain with the cavity volume (i.e. of the future catastrophic crack) created in the agglomerate has been deduced from the tomography images and is pictured in Figure 7e. Between 70%-120% nominal strain, the volume variation is almost negligible. Then, at higher strain, the cavity rapidly grows radially and its volume increases exponentially. When the cavity becomes a crack propagating in the matrix, its volume grows catastrophically. Tomography and SEM images (Figures 8a and 8b) confirm the above observation, with evidence of crack initiation from one critical defect (CB_{aggl}). However, a filled EPDM can also break due to multiple initiations as shown in Figure 9. In this case, the SEM image shows that cracks originate and propagate radially from the two CB_{aggl} observed. The 2 cracks eventually coalesce and this leads to the material rupture.

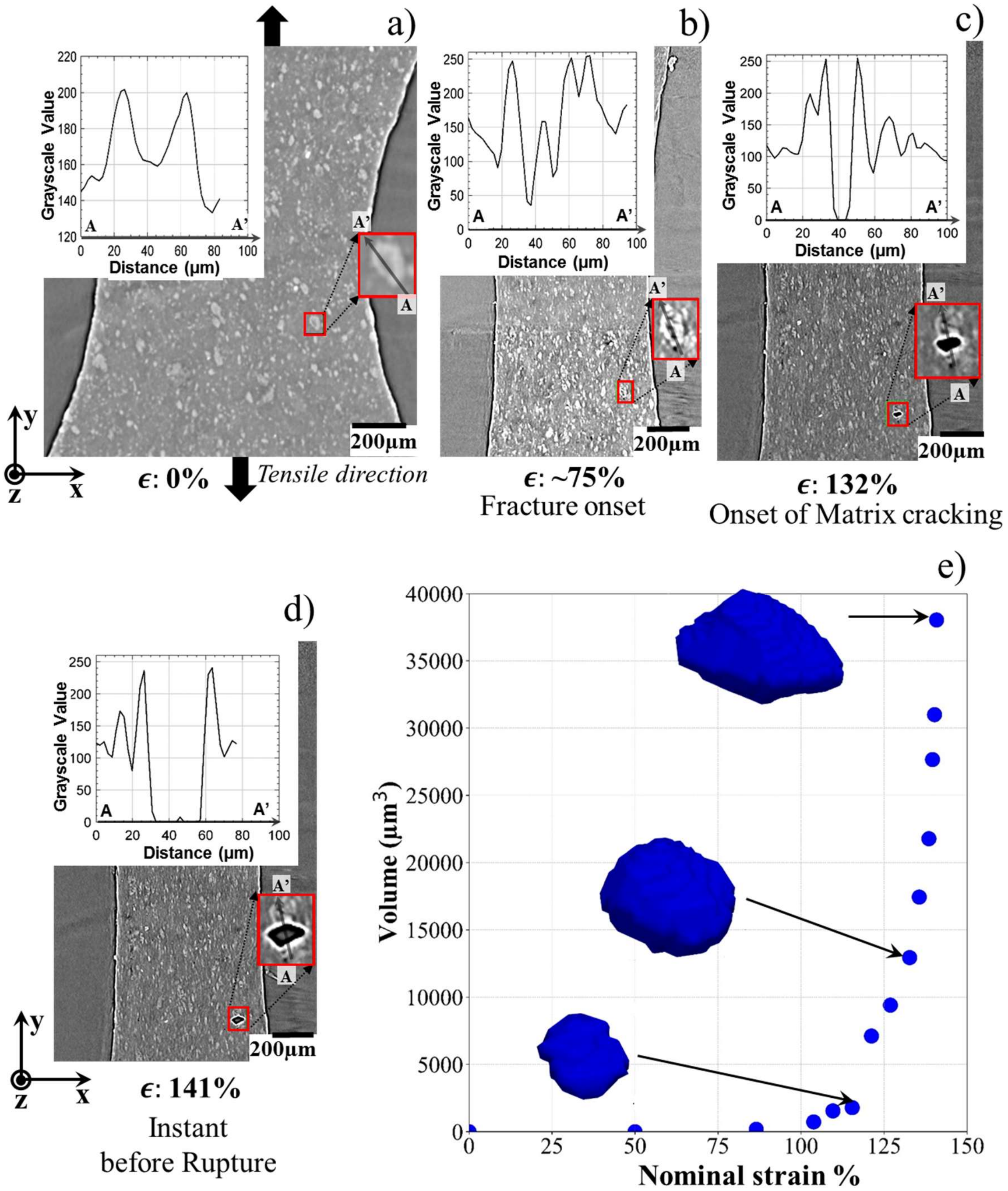

Figure 7: visualization of crack initiation in a filled EPDM, a)-d) microstructural evolution of the critical defect with nominal strain (ϵ). The inset photo in each figure shows a magnified CB$_{aggl.}$.b) onset of the fracture/cavitation inside the CB$_{aggl}$ at 75% nominal strain, c) onset of matrix cracking at 132% nominal strain, d) state of the crack just before sample rupture, e) volume of the cavity inside the agglomerate as a function of the macroscopic deformation.

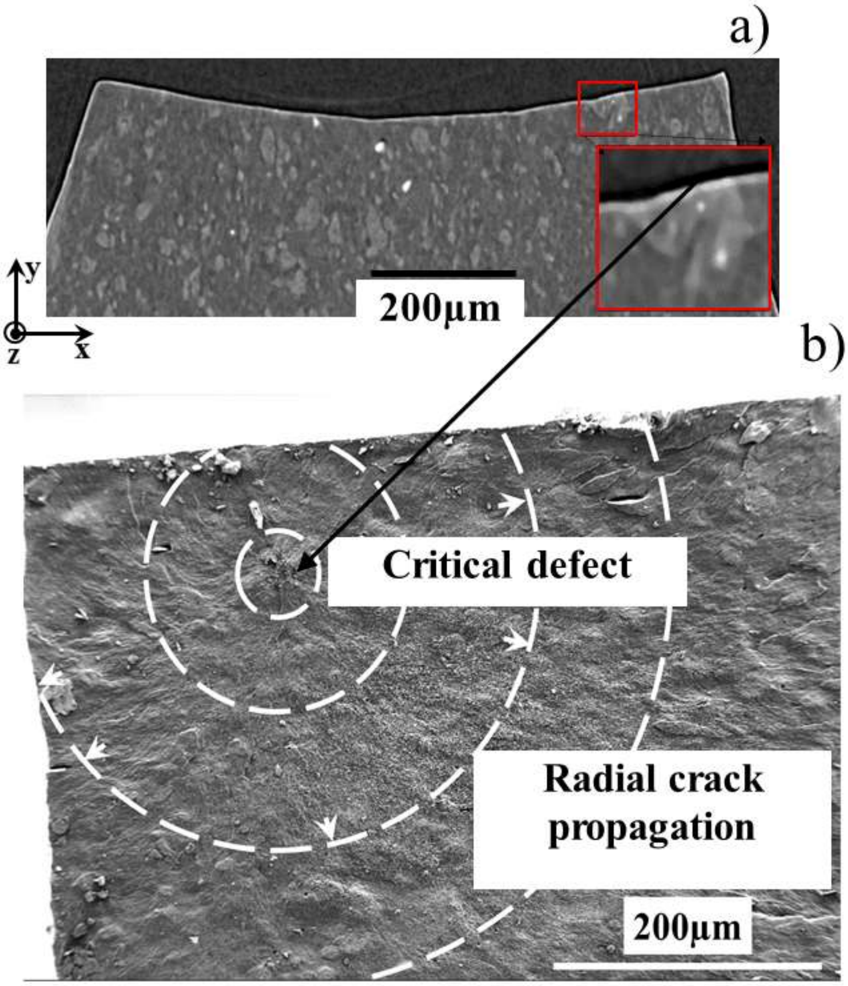

Figure 8: Continuation of Figure 8, a) slice view of the broken sample with the critical defect. The inset photo shows the magnified critical CB_{aggl}. B) SEM observation confirming the crack initiation and further propagation of the crack from the critical defect.

Even though other defects (metallic oxide particles) exist in the materials, crack always initiates from CB_{aggl} defect(s). Moreover, we can conclude from our observations that the crack initiation mechanism remains the same whatever the CB_{aggl} concentration in the material is (as shown in SI 7.4 for material with 4.3% of CB_{aggl}). It is worth noting to be complete that, there are exceptions to this when there is a surface defect such as a pre-existing cut at the surface edge due to improper die cutting of the samples (SI 7.5).

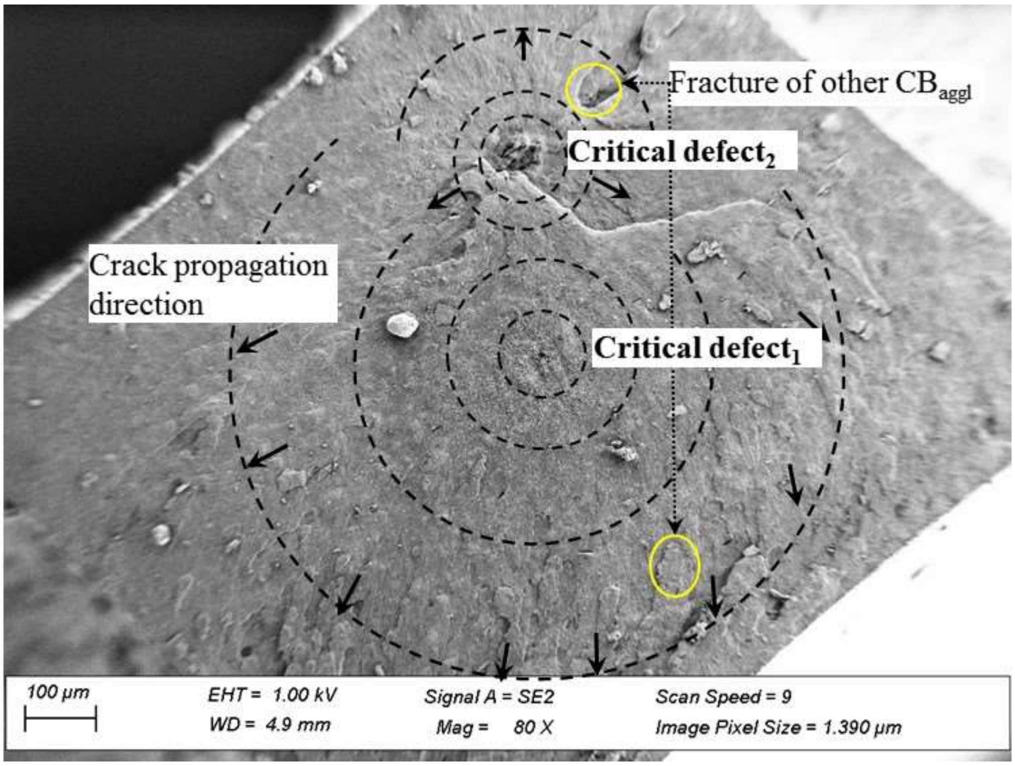

Figure 9: SEM observation of the ruptured surface of S_11.5.

4. DISCUSSION

The filled material presented in this chapter contains two types of defects – metallic oxide particles and CB$_{aggl}$. To understand their role on crack initiation mechanism, model materials with 3 different concentrations of CB$_{aggl}$ have been processed; the 1st material contains very high concentration of CB$_{aggl}$ (S_11.5 with 11.5% volume fraction), the 2nd material has CB$_{aggl}$ concentration representative of those commonly found in industrial production (4.3%) and the last material contains an intermediate CB$_{aggl}$ concentration between the former 2 model materials (9%). It is worth noting that we did not incorporate ZnO particles (commonly used in the industry) to avoid problems related to the non-visibility of CB$_{aggl}$ in their presence, as reported in some recent literature studies. However, the studied materials contain low concentrations (less than 0.05%) of pre-existing metallic oxide particles in the initial EPDM matrix (as usually observed in industrial materials). The mechanical properties characterization shows that despite their different concentrations of CB$_{aggl}$, all the model materials have similar rupture properties, i.e. similar strain and stress at break, which is a counterintuitive result. A micron-scale characterization of the material is performed to understand this result.

Crack initiation is due to the nucleation of damage and its final evolution to a matrix crack. Matrix decohesion occurs at the pole of the rigid metallic oxide particles when the material is stretched. This does not lead to crack initiation. For instance, a cavity formed from decohesion between the matrix and a particle with Eq_{diam} of 35µm does not rupture the material even when the material is stretched above 135% nominal strain. The created cavities mostly grow in parallel to the applied stress direction as shown in previous studies[10,33]. This might be due to lower tearing energy along the direction of applied stress compared to propagation in the perpendicular direction: for instance, in an NR matrix, the fracture strength required for the tear to grow in the direction of applied stress is about 40% less than the strength required for it to grow in the perpendicular direction[34,35]; the study concluded that this crack tends to stop. Thus, defects like metallic oxide particles are not critical for crack initiation; we confirmed this through the observation of rupture surfaces of different samples (see SI section 7.6). This is consistent with the observations made by Huneau *et al.*[8] regarding materials containing ZnO particles submitted to fatigue solicitation.

Conversely, CB_{aggl} can initiate cracks in the material upon stretching. Cavitation occurs inside the agglomerates. The dependence of the stress needed to observe this cavitation with power -0.5 of the agglomerate diameter suggests that it may originate from some decohesion mechanism at the interface between two of the layers (with different aggregates concentration) which form the agglomerates. In a second step, the cavity grows rapidly inside the CB_{aggl}. Not all CB_{aggl} transform their internal fracture into a crack in the matrix. To do so, their preferred location inside the sample is in a zone with larger strain, originating from the sample geometry. Moreover, when they undergo multiple internal fractures, this likely delays the propagation of the main internal cavity to the matrix (and therefore its transformation as a crack in a matrix). This was verified for all our model materials, using SRCT characterization combined with SEM analysis.

The morphology features of 9 critical CB_{aggl} that initiated crack are presented on Figure 10. Critical agglomerates in S_11.5 have larger structure factor compared to S_4.3 (due to more shearing energy provided to S_4.3 inside the internal mixer, as explained in previous article[23]),and they are more elongated, but this is also the case for all the agglomerates of S_11.5 when compared to those of S_4.3. Actually, the common feature of all the critical agglomerates, without distinction of the materials, is a minimum volume around 40000µm^3.

All these critical CB_{aggl} were also found to be closer to the surface edges. Indeed, due to the sample geometry, the strain at the edge is slightly larger compared to the specimen center. As an example, see Figure 11 where it is shown, for a specimen of S_9.0 stretched at 50% nominal strain , the region where the strain in the tensile direction is greater than 0.8 of the maximum strain and the position of the critical CB_{aggl} (marked in blue color).

Now, given the different CB_{aggl} concentration, these results also show that in the range of the tested concentrations, the quantity of CB_{aggl} is not important with respect to crack initiation (likely because the probability to find a critical agglomerate is large enough for all the tested materials). This is indirectly confirmed by results of tensile testing (Figure 4), which do not exhibit significant differences between the 3 materials.

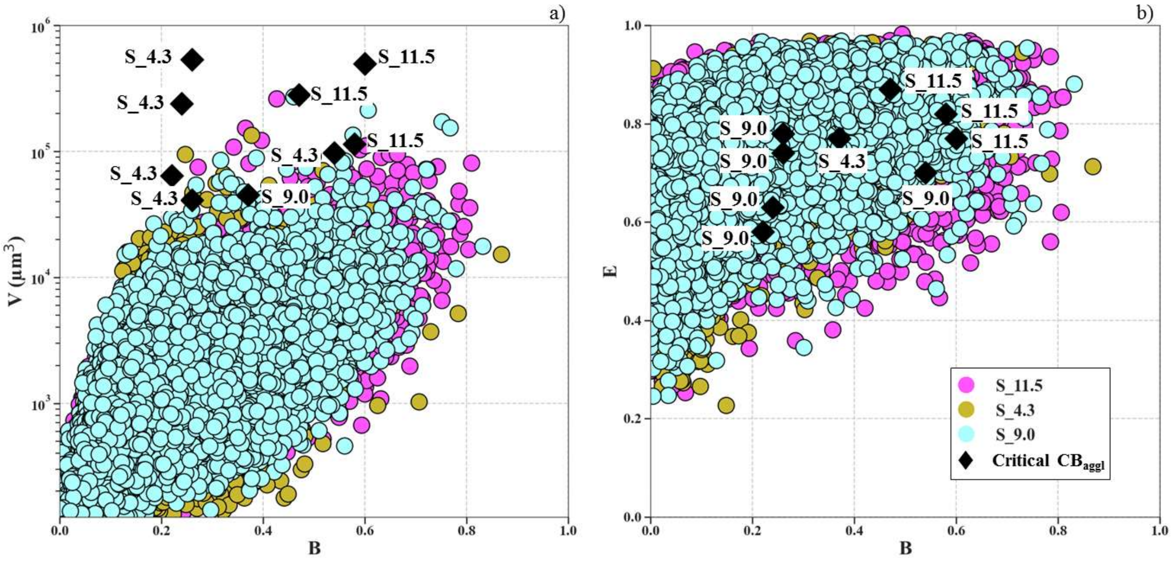

Figure 10: morphology features: a) V vs B and b) E vs B for materials S_11.5, S_4.3 and S_9.0. The black symbols characterize the morphology of the critical defects found in these materials.

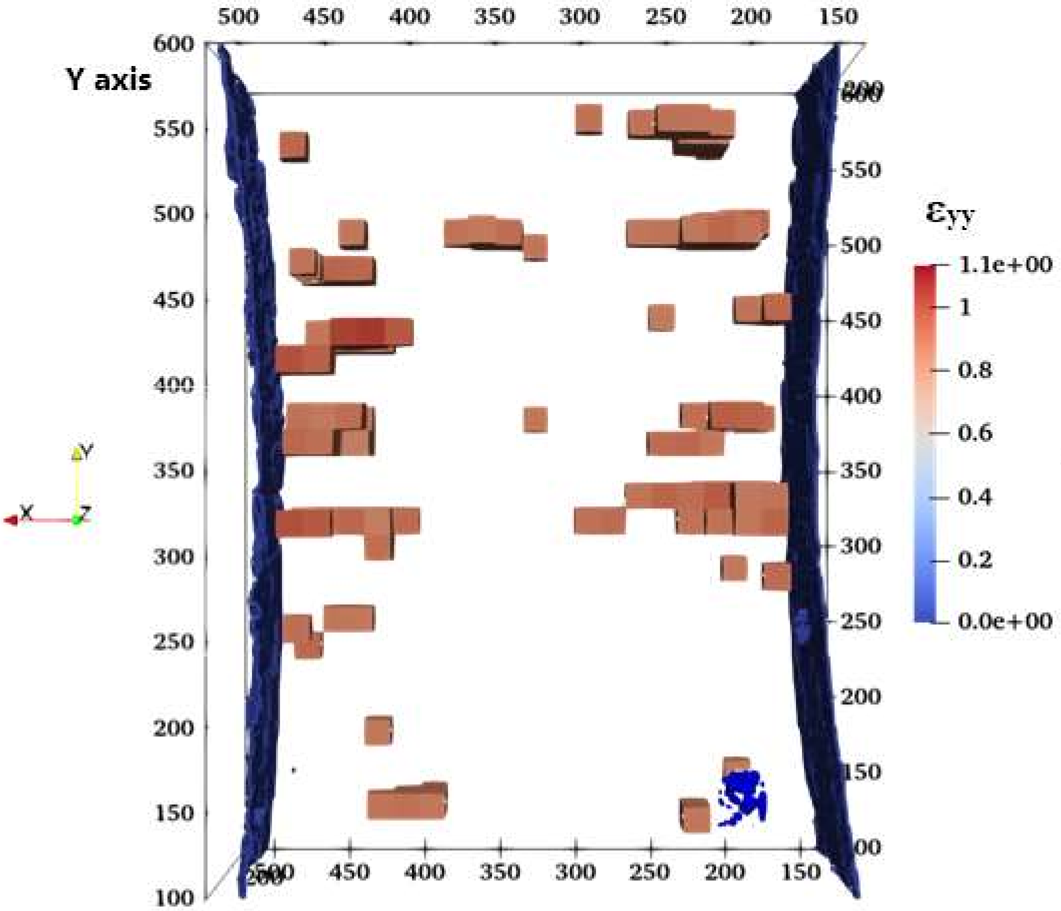

Figure 11: Strain field for model material S_9.0 in the direction of applied stress, at a 50% nominal strain. The colored areas are those where local strain is greater than 80% of the maximal strain. "ϵ_{yy}" is the name of the strain applied in the tensile direction. Each cube is of the size 16 voxel (1 voxel=2.19µm^3).

After crack initiation, crack propagates and ruptures the material. A previous work[17]showed that the crack propagation resistance of S_11.5 is higher than S_4.3 at high strain energy release rate (G). However, the ultimate properties of these materials remain the same in a tensile specimen geometry. At high G (high strain) crack propagation speed is in the order of magnitude of 10^{-4} m/s. Note that G increases with the strain and the crack size. Therefore the sample breaks too fast to see any differentiation in the rupture properties between the materials. Thus, in this geometry during tensile test, rupture properties are governed by the crack initiation mechanism.

5. CONCLUSION

An in-situ tensile study using SRCT on a filled EPDM shows the damage (here mainly void formation) and the crack initiation mechanisms associated to different defects which act differently upon stretching the material. We demonstrated that the mechanism associated to defects like metallic oxide particles is decohesion and the stress for its onset depends on their size. The power law dependence between applied stress and particle size requires further studies, which would take into account the debonded area, adhesion energy etc… In any case, the metallic particles are not critical defects in the studied materials and the cavities they bring about grow in the direction of the applied stress rather than perpendicular to it. On the other hand, CB_{aggl} are found to be critical defects for crack initiation. The first step is nucleation of a cavity inside the agglomerate. This cavity is actually formed by the debonding of polymer layer from the aggregates layers. However, this needs to be further explored through a nanoscale characterization for better understanding of the nucleation mechanisms of these cavities inside CB_{aggl}. The nucleated cavity grows as the fractured CB_{aggl} undergoes further deformation, and then propagates into the matrix, which triggers rupture of the material. However, all the CB_{aggl} that fracture do not lead to a crack propagating in the matrix. Only those with size bigger than 40000 μm^3 and in the more deformed zone of the specimen (close to the edges of the sample in our test) initiate a critical crack. Evaluating the specific contribution of the agglomerates position would need the help of mechanical simulation, which could be a another nice prospect of this experimental work.

6. ACKNOWLEDGEMENTS

This work was supported by LRCCP and ANRT (CIFRE N° 2018 /0429). Parts of this research were carried out PETRA III P05 beamline at DESY, Germany (operated by Helmholtz-Zentrum Hereon). We would like to thank the beamline staff for assistance in conducting the experiments. Some parts of the study were also carried out at ANATOMIX beamline at Soleil. ANATOMIX is an Equipment of Excellence (EQUIPEX) funded by the Investments for the Future program of the French National Research Agency (ANR), project NanoimagesX, grant no. ANR-11-EQPX-0031.

7. SUPPORTING INFORMATION

7.1 Onset of damage mechanism for ZnO

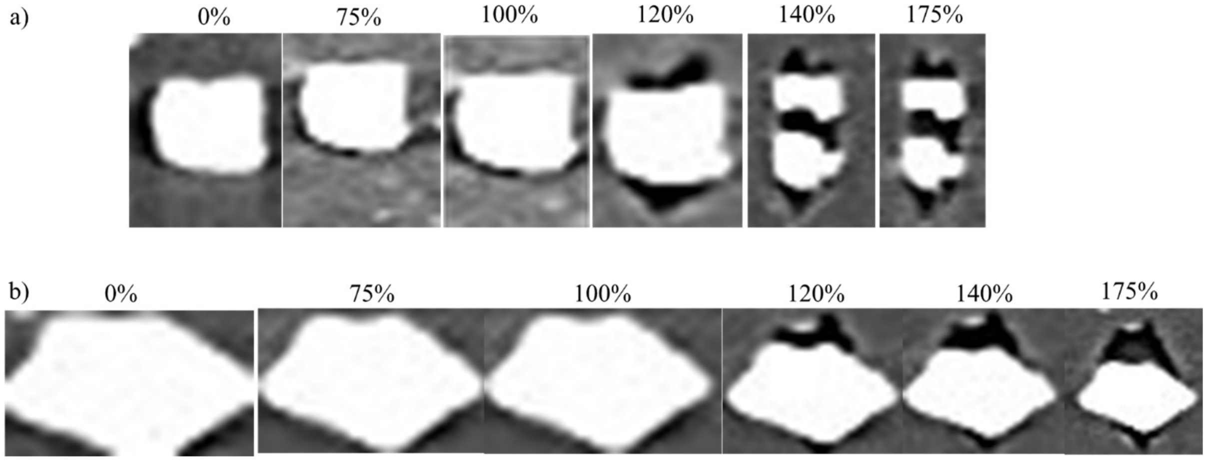

Figure A1: Damage evolution in a material containing 3% volume fraction of ZnO. A) at 120% nominal strain, there is a decohesion at the poles followed by fracture of ZnO at 140% nominal strain. B) decohesion at the poles of ZnO inclusion at 120% nominal strain, without subsequent fracture of the inclusion.

7.2 Growth of cavity volume for a metallic inclusion with size =23µm

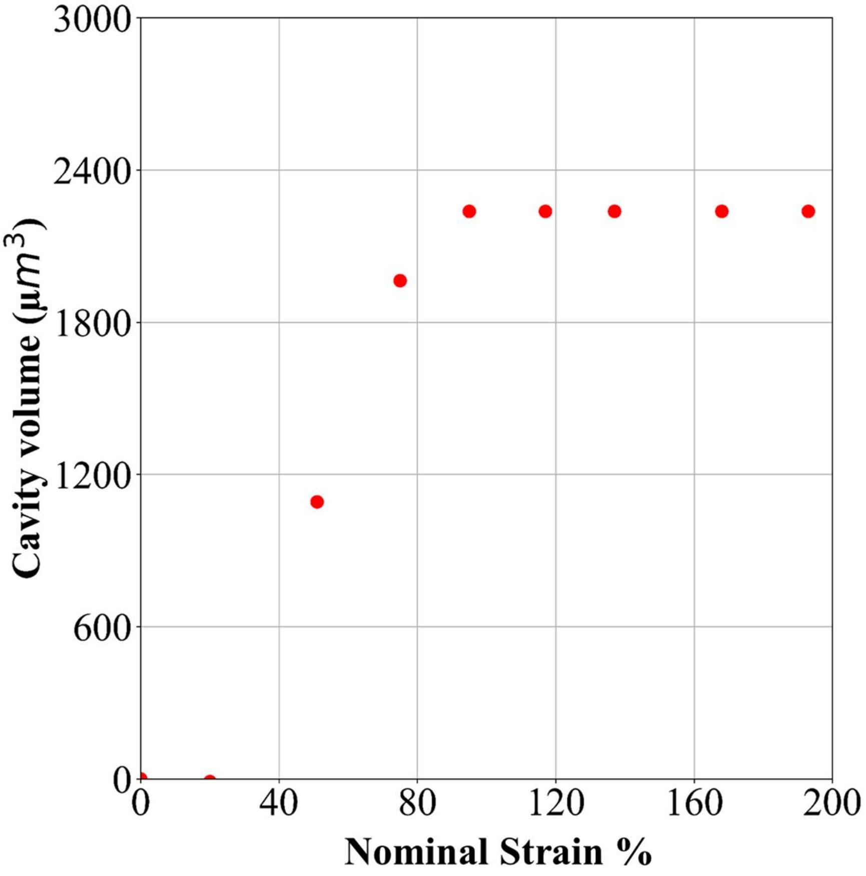

Figure A2: Evolution of cavity associated to a defect with Eq_{diam}= 23µm

7.3 S_9.0 damage mechanism of CB_{aggl}

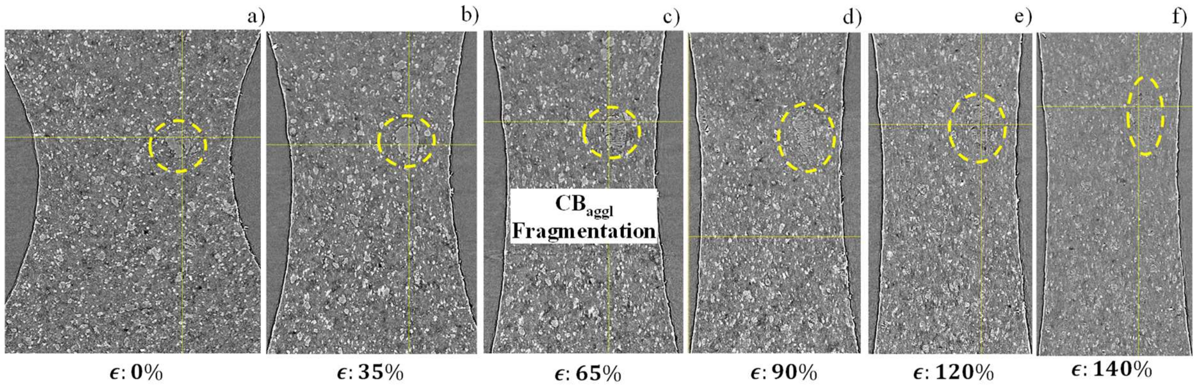

Figure A3: a)-f) evolution of CB_{aggl} during a tensile test in material S_9.0 observed using SRCT. CB_{aggl} are fractured between 35%-65%, to be precise at 40% nominal strain. CB_{aggl} undergo multiple fragmentations as the macroscopic deformation increases.

7.4 S_4.3 damage mechanism

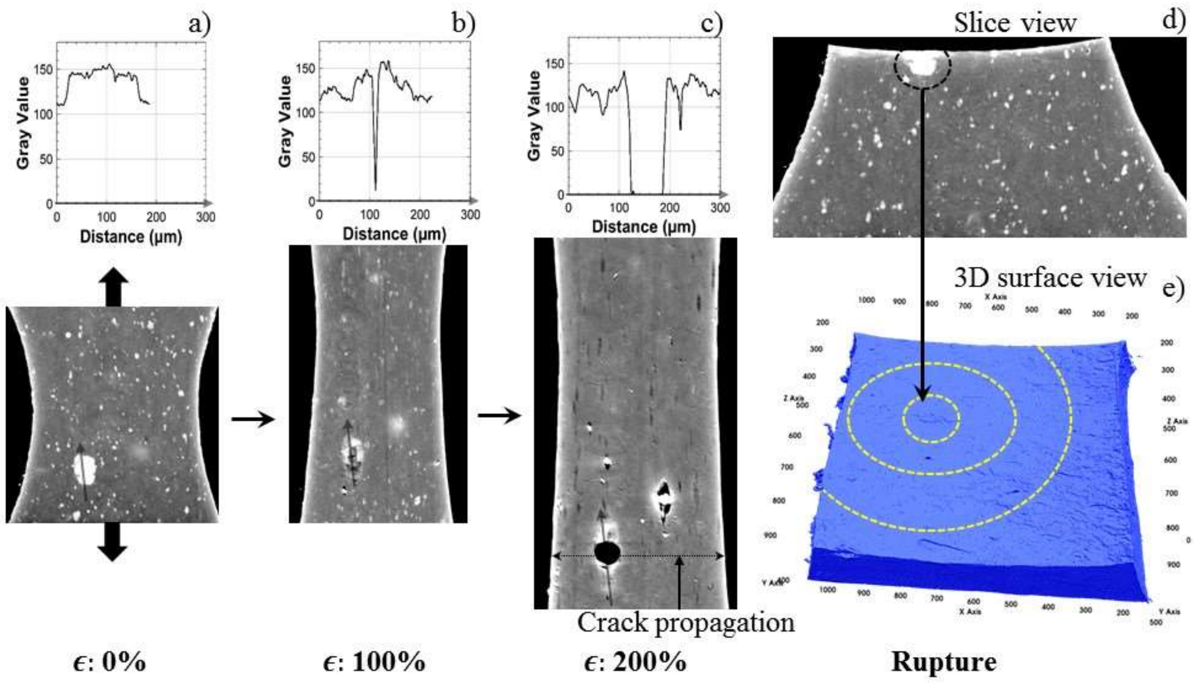

Figure A4: Crack initiation mechanism for S_4.3

7.5 Images of the CB_{aggl} in the edges

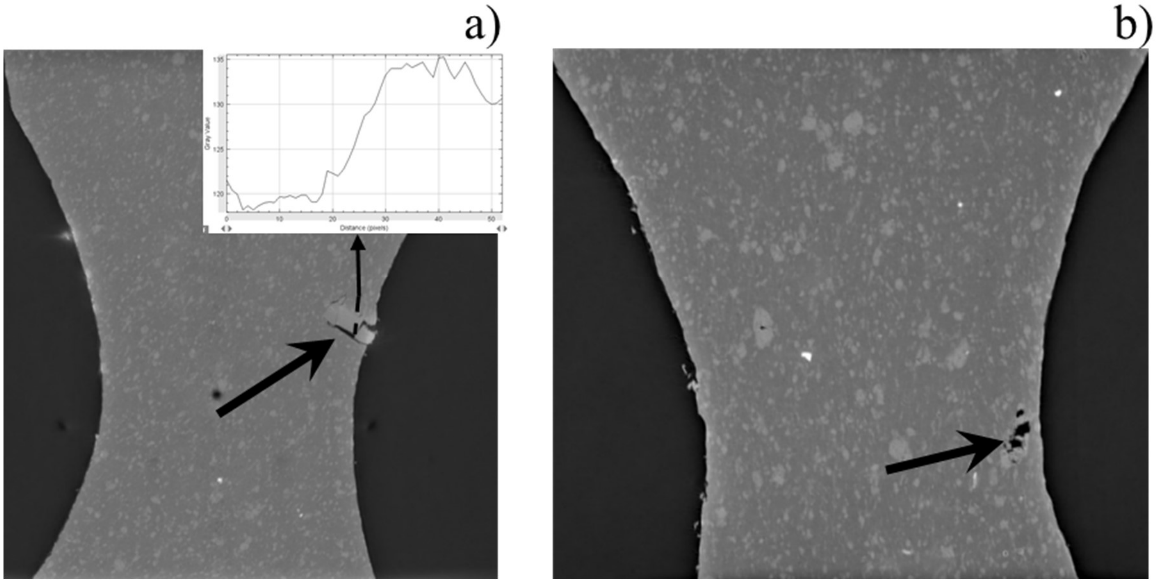

Figure A5: Slice images showing critical defects. The defects pointed in the images are CB_{aggl}

7.6 Material Rupture surfaces

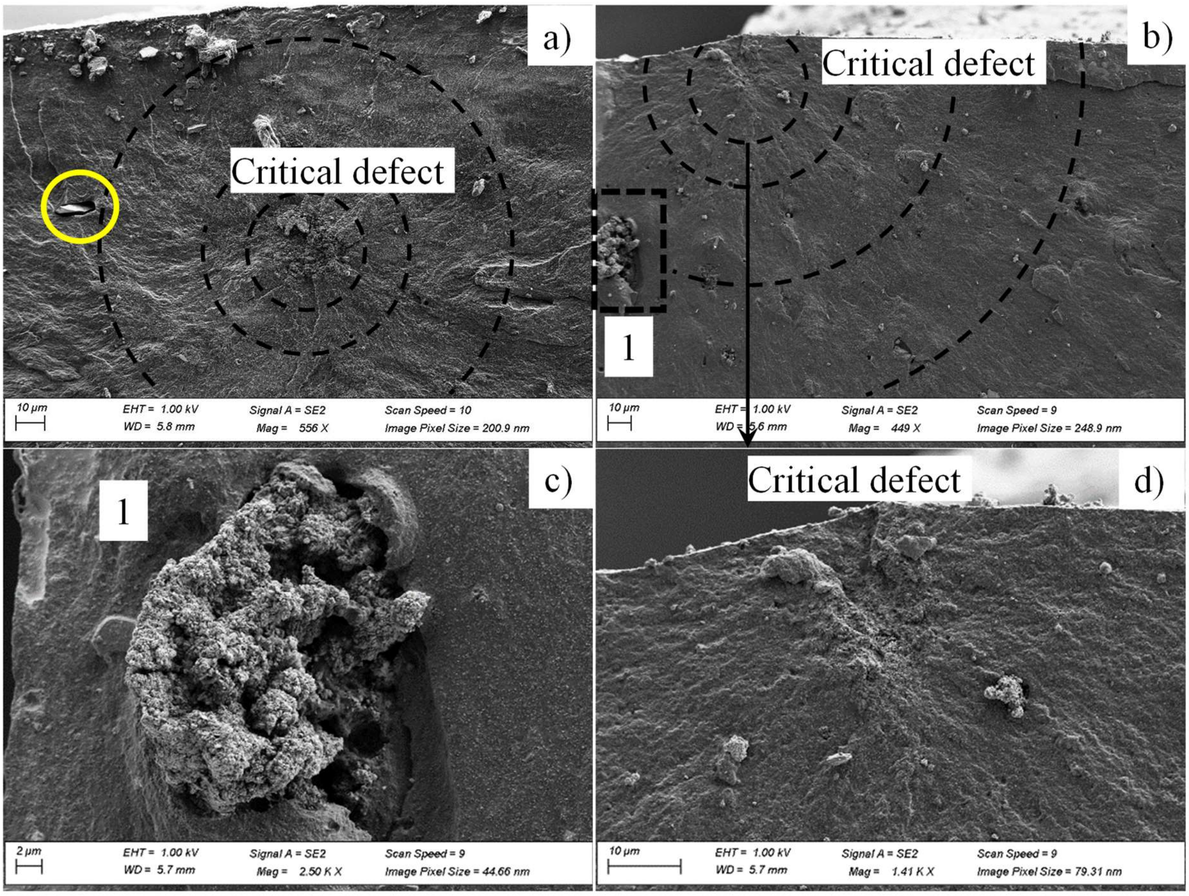

Figure A6: SEM image showing the rupture surface of S_9.0, a) decohesion at the inclusion, marked by a yellow circle next to the critical defect, b) rupture surface and critical defect (CBaggl) in a material containing ZnO. c) and d) enlarged views of a ZnO inclusion (rectangle 1) and of the critical defect from picture b).

8. REFERENCES

[1] Medalia AI, Heckman FA. Morphology of aggregates. VII. Comparison chart method for electron microscopic determination of carbon black aggregate morphology. J Colloid Interface Sci 1971;36:173–90. https://doi.org/10.1016/0021-9797(71)90162-7.

[2] Medalia A. Effect of Carbon Black on Ultimate Properties. Rubber Div Am Chem Soc 1987;60:45–60.

[3] Dizon ES, Hicks AE, Chirico VE. The Effect of Carbon Black Parameters on the Fatigue Life of Filled Rubber Compounds. Rubber Chem Technol 1974;47:231–49. https://doi.org/10.5254/1.3540429.

[4] Astruc M. Étude rhéo-optique des mécanismes de dispersion de mélanges sous cisaillement simple . 1 Mélanges concentrés de polymères immiscibles . 2 Mélanges polymères-charges poreuse. l'École des Mines de Paris, 2008. https://doi.org/tel-00275370.

[5] Collin V, Boudimbou I, Peuvrel-Disdier E. New insights in dispersion mechanisms of carbon black in a polymer matrix under shear by rheo-optics. J Appl Polym Sci

2013;127:2121–31. https://doi.org/10.1002/app.37769.

[6] Le Cam J-B, Huneau B, Verron E. Fatigue damage in carbon black filled natural rubber under uni- and multiaxial loading conditions. Int J Fatigue 2013;52:82–94. https://doi.org/10.1016/j.ijfatigue.2013.02.022.

[7] Le Saux V, Marco Y, Calloch S, Charrier P. Evaluation of the fatigue defect population in an elastomer using X-ray computed micro-tomography. Polym Eng Sci 2011;51:1253–63. https://doi.org/10.1002/pen.21872.

[8] Huneau B, Masquelier I, Marco Y, Le Saux V, Noizet S, Schiel C, et al. Fatigue crack initiation in a carbon black-filled natural rubber. Rubber Chem Technol 2016;89:126–41. https://doi.org/10.5254/rct.15.84809.

[9] Glanowski T, Marco Y, Le Saux V, Huneau B, Champy C, Charrier P. Fatigue crack initiation around inclusions for a carbon black filled natural rubber: an analysis based on micro-tomography. In: Huneau B, Le Cam J-B, Marco Y, Verron E, editors. Const. Model. Rubber XI, CRC Press; 2019, p. 368–73. https://doi.org/10.1201/9780429324710-64.

[10] Gent AN, Park B. Failure processes in elastomers at or near a rigid spherical inclusion. J Mater Sci 1984;19:1947–56. https://doi.org/10.1007/BF00550265.

[11] Zhuk A V., Knunyants NN, Oshmyan VG, Topolkaraev VA, Berlin AA. Debonding microprocesses and interfacial strength in particle-filled polymer materials. J Mater Sci 1993;28:4595–606. https://doi.org/10.1007/BF00414247.

[12] Gent AN. Detachment of an elastic matrix from a rigid spherical inclusion. J Mater Sci 1980;15:2884–8. https://doi.org/10.1007/BF00550559.

[13] Lefèvre V, Ravi-Chandar K, Lopez-Pamies O. Cavitation in rubber: an elastic instability or a fracture phenomenon? Int J Fract 2015;192:1–23. https://doi.org/10.1007/s10704-014-9982-0.

[14] Maire E, Le Bourlot C, Adrien J, Mortensen A, Mokso R. 20 Hz X-ray tomography during an in situ tensile test. Int J Fract 2016;200:3–12. https://doi.org/10.1007/s10704-016-0077-y.

[15] Maire E, Withers PJ. Quantitative X-ray tomography. Int Mater Rev 2014;59:1–43. https://doi.org/10.1179/1743280413Y.0000000023.

[16] Wilde F, Ogurreck M, Greving I, Hammel JU, Beckmann F, Hipp A, et al. Micro-CT at the imaging beamline P05 at PETRA III, 2016, p. 030035. https://doi.org/10.1063/1.4952858.

[17] Kallungal J, Chazeau L, Chenal J-M, Adrien J, Maire E, Barrès C, et al. Crack propagation in filled elastomers: 3D study of mechanisms involving the filler agglomerates. Eng Fract Mech 2022;274:108771. https://doi.org/10.1016/j.engfracmech.2022.108771.

[18] Moosmann J, Ershov A, Weinhardt V, Baumbach T, Prasad MS, LaBonne C, et al. Time-lapse X-ray phase-contrast microtomography for in vivo imaging and analysis of morphogenesis. Nat Protoc 2014;9:294–304. https://doi.org/10.1038/nprot.2014.033.

[19] Weitkamp T, Scheel M, Perrin J, Le Roux V, Joyet V, Chaouchi S, et al. Progress in Microtomography at the ANATOMIX Beamline of Synchrotron Soleil. Microsc Microanal 2018;24:246–7. https://doi.org/10.1017/s1431927618013570.

[20] Weitkamp T, Scheel M, Perrin J, Daniel G, King A, Roux L, et al. Microtomography on the ANATOMIX beamline at Synchrotron SOLEIL 2020.

[21] Kallungal J, Chazeau L, Chenal J-M, Adrien J, Maire E, Barres C, et al. Methodology for 3D characterization of microstructural defects in filled polymer using X-ray Tomography. Const. Model. Rubber XI, CRC Press; 2019, p. 77–81. https://doi.org/10.1201/9780429324710-14.

[22] Paganin D, Mayo SC, Gureyev TE, Miller PR, Wilkins SW. Simultaneous phase and

amplitude extraction from a single defocused image of a homogeneous object. J Microsc 2002;206:33–40. https://doi.org/10.1046/j.1365-2818.2002.01010.x.

[23] Kallungal J, Chazeau L, Chenal J-M, Adrien J, Maire E, Barrès C, et al. Quantitative analysis of carbon black agglomerate morphology in elastomer composites based on X-ray Tomography by means of numerical clustering. Rubber Chem Technol, 2022, in press.

[24] van der Walt S, Schönberger JL, Nunez-Iglesias J, Boulogne F, Warner JD, Yager N, et al. scikit-image: image processing in Python. PeerJ 2014;2:e453. https://doi.org/10.7717/peerj.453.

[25] Lachambre J. Développement d'une Méthode de Caractérisation 3D des Fissures de Fatigue à l'aide de la Corrélation d'Images Numériques obtenues par Tomographie X. l'Institut National des Sciences Appliquées de Lyon, 2014.

[26] Roux S, Hild F, Viot P, Bernard D. Three-dimensional image correlation from X-ray computed tomography of solid foam. Compos Part A Appl Sci Manuf 2008;39:1253–65. https://doi.org/10.1016/j.compositesa.2007.11.011.

[27] Huneau B, Masquelier I, Marco Y, Saux V Le, Noizet S, Schiel C, et al. Initiation mechanisms of fatigue cracks in carbon black filled natural rubber. Const. Model. Rubber IX, 2015. https://doi.org/doi:10.1201/b18701-69.

[28] Gent AN, Park B. Failure processes in elastomers at or near a rigid spherical inclusion. J Mater Sci 1984;19:1947–56. https://doi.org/10.1007/BF00550265.

[29] Robertson CG, Stoček R, Mars W V. The Fatigue Threshold of Rubber and Its Characterization Using the Cutting Method, 2020, p. 57–83. https://doi.org/10.1007/12_2020_71.

[30] Abraham F, Clauß G, Alshuth T. Testing and simulation of the influence of glass spheres on fatigue life and dynamic crack propagation of elastomers. In: Per-Erik Austrell, editor. Const. Model. Rubber IV, Taylor & Francis; 2005, p. 6.

[31] Fond C. Cavitation criterion for rubber materials: A review of void-growth models. J Polym Sci Part B Polym Phys 2001. https://doi.org/10.1002/polb.1183.

[32] Selles N, Cloetens P, Proudhon H, Morgeneyer TF, Klinkova O, Saintier N, et al. Voiding Mechanisms in Deformed Polyamide 6 Observed at the Nanometric Scale. Macromolecules 2017;50:4372–83. https://doi.org/10.1021/acs.macromol.7b00727.

[33] Cho K, Gent AN, Lam PS. Internal fracture in an elastomer containing a rigid inclusion. J Mater Sci 1987;22:2899–905. https://doi.org/10.1007/BF01086488.

[34] Gent AN, Kim HJ. Tear Strength of Stretched Rubber. Rubber Chem Technol 1978;51:35–44. https://doi.org/10.5254/1.3535725.

[35] Gent AN, Razzaghi-Kashani M, Hamed GR. Why do cracks turn sideways? Rubber Chem Technol 2003;76:122–30. https://doi.org/10.5254/1.3547727.